

A comparison of freehand three-dimensional ultrasound reconstruction techniques

Robert Rohling¹, Andrew Gee^{1*} and Laurence Berman²

¹Department of Engineering, Trumpington Street, Cambridge CB2 1PZ, UK

²Department of Radiology, Addenbrooke's Hospital, Cambridge CB2 2QQ, UK

Abstract

Three-dimensional freehand ultrasound imaging produces a set of irregularly spaced B-scans, which are typically reconstructed on a regular grid for visualization and data analysis. Most standard reconstruction algorithms are designed to minimize computational requirements and do not exploit the underlying shape of the data. We investigate whether an approximation with splines holds any promise as a better reconstruction method. A radial basis function approximation method is implemented and compared with three standard methods. While the radial basis approach is computationally expensive, it produces accurate reconstructions without the kind of visible artefacts common with the standard methods. The other potential advantages of radial basis functions, such as the direct computation of derivatives, make further investigation worthwhile.

Keywords: 3-D ultrasound imaging, interpolation, radial basis function

Received July 23, 1998; revised April 1, 1999; accepted April 2, 1999

1. INTRODUCTION

Ultrasound is a widely used imaging modality that has a large variety of clinical applications. Conventional two-dimensional (2-D) diagnostic imaging is performed with a hand-held probe which transmits ultrasound pulses into the body and receives the echoes. The magnitude and timing of the echoes are used to create a 2-D grey-level image (B-scan) of a cross-section of the body in the scan plane. Three-dimensional (3-D) ultrasound imaging extends this concept, so that a volume of intensity data is created from pulse-echo information.

There are several methods of performing 3-D ultrasound imaging (Fenster and Downey, 1996). One method, freehand imaging, makes use of conventional ultrasound technology to build up a 3-D data set from a number of 2-D B-scans acquired in rapid succession. This is achieved by attaching a 3-D position sensor to the probe, so that each B-scan can be labelled with the position and orientation of the scan plane. The physician then moves the probe slowly and steadily over a particular anatomical region, so that the set of acquired

B-scans encompasses the volume of interest with few gaps. Figure 1 shows the elements of a 3-D freehand system.

While the set of B-scans can be reviewed individually, reconstructing them into a regular array makes it possible to use conventional 3-D visualization and data analysis tools. These tools include any-plane reslicing, volume rendering, surface rendering, segmentation and registration procedures. The reconstruction step is important because any loss of image quality or the introduction of artefacts must be avoided. For example, a small loss in image quality during reconstruction can make a barely detectable pathology in a B-scan become undetectable in the reconstructed data. This may result in a misdiagnosis. In this paper, we survey existing reconstruction techniques and propose a new technique based on a functional approximation.

The paper is organized as follows. In Section 2, the existing reconstruction methods are reviewed and the new reconstruction method is described. In Section 3, the acquisition system, two *in vivo* examinations and a series of comparative tests are described. The results, followed by a discussion of the relative merits of the various techniques, are given in Section 4. Finally, conclusions and suggestions for future work are given in Section 5.

*Corresponding author
(e-mail: ahg@eng.cam.ac.uk)

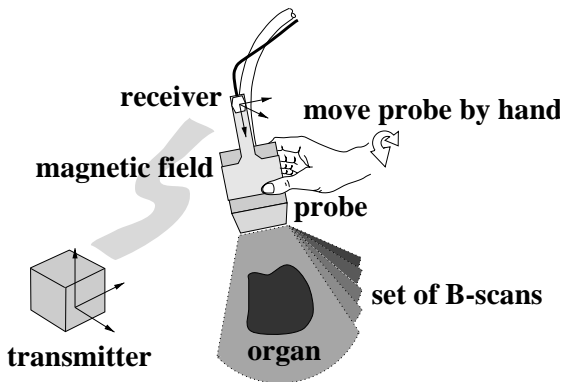


Figure 1. 3-D freehand ultrasound imaging. Freehand imaging allows the physician to move the probe freely so the B-scans can have arbitrary relative locations and may overlap each other. As the probe moves, the B-scans are captured and stored in computer memory. A magnetic position sensor measures the position of a receiver (mounted on the probe) relative to a transmitter (fixed with respect to the patient's body). The relative location of each scan plane is then calculated and the B-scans combined into a single volume of data.

2. RECONSTRUCTION METHODS

2.1. Overview

Since the motion of the probe in freehand imaging is controlled by the physician, the B-scans can be at any relative position and orientation. This means that the pixels (B-scan elements) lie at irregular locations in the array of voxels (volume elements). Therefore, the reconstruction problem can be classified as unstructured, or scattered, data interpolation^a (Nielson, 1993).

A survey of the literature reveals a number of different methods for reconstruction of 3-D freehand ultrasound data sets. Most of these methods are very simple because they are designed to minimize the time and memory required for reconstruction. This is because physicians want to visualize the 3-D data sets immediately after acquisition, so the reconstruction should ideally take only a few seconds. Although almost all freehand systems perform reconstruction at some stage, details of the reconstruction method are often unpublished since the method is considered *ad hoc*. Nevertheless, the methods that have been published can be classified into the following categories: voxel nearest-neighbour (VNN) interpolation, pixel nearest-neighbour (PNN) interpolation and distance-weighted (DW) interpolation.

^aSince the pixels all lie on planes, the data are actually best described as semi-structured.

2.2. Voxel nearest-neighbour interpolation

The concept of VNN interpolation is easy to understand: each voxel is assigned the value of the nearest pixel. There are no parameters to set. A naive implementation would traverse the array one voxel at a time and calculate the value of the nearest pixel, but this would be computationally inefficient. Using the fact that the nearest pixel lies along a line normal to the nearest B-scan greatly speeds up the reconstruction, making it one of the fastest of all methods. Moreover, a new 3-D ultrasound imaging system, developed at the University of Cambridge (Prager *et al.*, 1999), can rapidly produce slices of the set of B-scans without reconstructing an entire voxel array. By cleverly using the VNN interpolation method with dedicated graphics hardware, slices can be generated interactively.

While this reconstruction method has the advantage of avoiding gaps in the voxel array, reconstruction artefacts can be observed in slices through the voxel array. When a slice plane intersects several of the original B-scans, we can consider the interpolated image as a collage of projections from the intersected B-scans. Registration errors, including tissue motion and sensor errors, contribute to slight misalignment of the B-scans. This results in a piece of the collage slightly mismatching its neighbours. The lines of intersection between the pieces then become visible (see Figure 2a).

2.3. Pixel nearest-neighbour interpolation

Pixel nearest-neighbour interpolation is one of the most popular reconstruction methods (McCann *et al.*, 1988; Hottier and Collet Billon, 1990; Fine *et al.*, 1991; Nelson and Pretorius, 1997; Rohling *et al.*, 1997). The basic algorithm consists of two stages. In the first stage, the algorithm simply runs through each pixel in every B-scan and fills the nearest voxel with the value of that pixel. Multiple contributions to the same voxel are usually averaged, although the maximum value has also been suggested (Nelson and Pretorius, 1997). The parameters to set at this stage are therefore the weights on the multiple contributions.

If the voxel size is small compared to the distance between the acquired B-scans, gaps can occur in the voxel array. In practice, this situation is inevitable with voxel arrays of similar resolution to the B-scans. The second stage fills these remaining gaps in the voxel array. A variety of methods have been used, including averaging of filled voxels in a local neighbourhood (McCann *et al.*, 1988; Nelson and Pretorius, 1997) and interpolating between the two closest non-empty voxels in the transverse direction to the B-scans (Hottier and Collet Billon, 1990). Other publications (Fine *et al.*, 1991; Rohling *et al.*, 1997) do not describe the method for filling gaps, so we assume that they adopt similar approaches or

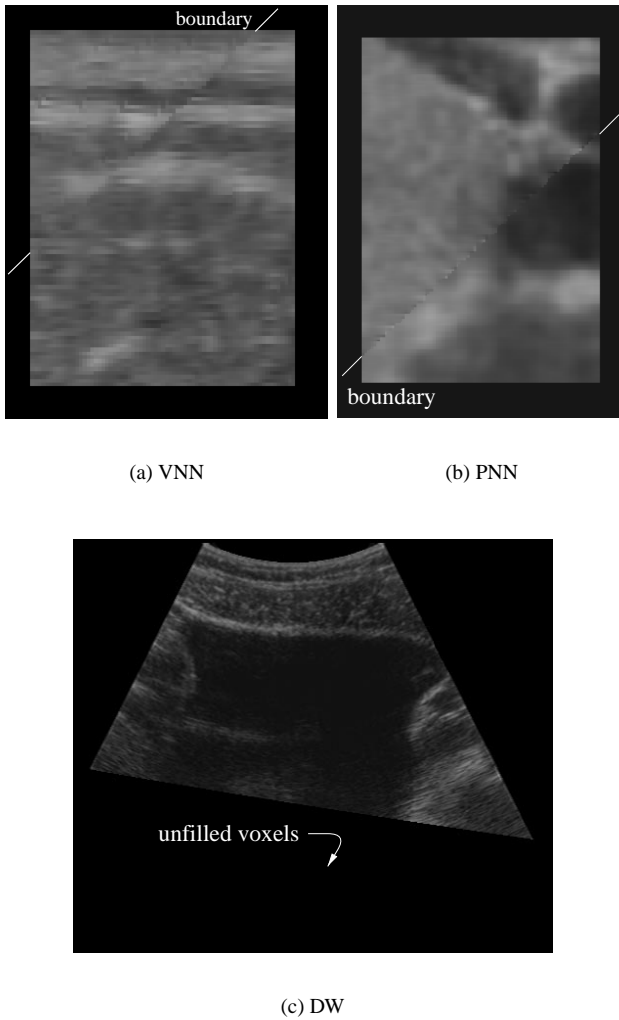


Figure 2. Reconstruction artefacts. In (a) a VNN interpolation is used to reconstruct an examination of the neck. A small slice of the voxel array is shown. The slight misalignment between the projections of the two nearest B-scans arises from registration errors. In (b) a PNN interpolation is used to reconstruct an examination of the thyroid. The boundary between the voxels filled by the first ‘bin-filling’ stage and voxels filled by the second ‘hole-filling’ stage is evident. In (c) a DW interpolation is used to reconstruct an examination of the bladder. The slice is truncated because the neighbourhood for selecting points is set too small, leaving some voxels unfilled.

choose the voxel size to be sufficiently large to avoid gaps. The parameters to set at this stage are the weights of the nearby voxels used to fill the gaps.

In summary, this method can be considered as a two-stage process: the first stage of ‘bin-filling’ the voxel array

with pixels is very fast, but the ‘hole-filling’ second stage may take longer, depending on the particular method chosen. Unfortunately, artefacts can be generated by this two-stage process. For example, a slice passing through regions of both first- and second-stage filled voxels may show the boundary between the highly detailed ‘bin-filled’ voxels and the smoothed ‘hole-filled’ voxels (see Figure 2b).

2.4. Distance-weighted interpolation

Like the VNN interpolation method, DW interpolation proceeds voxel by voxel. But, instead of using the nearest pixel, each voxel value is assigned the weighed average of some set of pixels from nearby B-scans. The parameters to choose are the weight function and the size and shape of the neighbourhood.

The simplest approach is to consider a fixed spherical neighbourhood of radius R , centred about each voxel (Barry *et al.*, 1997). All pixels in this neighbourhood are weighted by the inverse distance to the voxel and then averaged. This is similar to Shepard’s method (Shepard, 1968). Unfortunately, it has the disadvantage of not reproducing any of the local shape properties implied by the data because the resulting interpolant typically has local extrema at the data sites (Nielson, 1993). It also requires R to be set prior to reconstruction. If R is set too small, gaps may result (see Figure 2c). Such gaps are not necessarily undesirable: it may be better to leave gaps in the voxel array, indicating that the scanning sweep missed this particular location, instead of interpolating data at a considerable distance from where any was actually sampled. If R is set too large, the voxel array will appear highly smoothed, since the effect of inverse distance weighting can be quickly overwhelmed by the much larger number of data points falling into the larger local neighbourhood. Nevertheless, with dense B-scans and a small value of R , excellent results are claimed (Barry *et al.*, 1997).

Another DW interpolation method uses a non-uniformly shaped neighbourhood to account for the asymmetric shape of the point spread function of the ultrasound beam (Ohbuchii *et al.*, 1992). Essentially, the resolution is much higher within the B-scan than between the B-scans, so the authors create a ‘thick’ B-scan by convolving the 2-D B-scan image with a truncated 3-D Gaussian kernel. The 3-D Gaussian kernel is chosen to be wide perpendicular to the B-scan and narrow within the B-scan plane. A similar ‘thick’ slab of weight values of the truncated 3-D Gaussian kernel is computed. The voxel array accumulates both weight and intensity values separately, at those voxels intersected by the ‘thick’ B-scans.^b The final voxel intensity values are

^bThe authors also include a third value related to the ‘age’ of the intensity value, so that new overlapping B-scans will overwrite old B-scan values.

calculated by dividing the accumulated pixel intensity values by the accumulated weight values stored at that voxel. In summary, each voxel value represents a weighted average of nearby B-scans, with an asymmetric Gaussian weight function attached to each B-scan. While this method has the advantage of being incremental, gaps may still remain if the truncated Gaussian weight function is smaller than the gaps between B-scans (though, as discussed above, this is not necessarily an undesirable artefact).

Another DW method which uses a non-uniform neighbourhood is based on pairwise B-scan grouping (Trobaugh *et al.*, 1994). In this method, each voxel is filled only by the nearest two B-scans which fall on either side of it. For each of the two B-scans, lines are drawn perpendicular to the B-scan plane, passing through the voxel. Bilinear interpolation within each B-scan determines the contributing pixel value from that B-scan. The voxel is then set to the inverse DW average of the two contributing pixel values. This method has the advantage of retaining the resolution of each B-scan in the voxel array and avoiding gaps. Although it is clear which pairs of B-scans to use with simple motions, such as linear sweeps, it is not clear which pairs to use with more arbitrarily located B-scans. It has been suggested that the pairs be chosen time sequentially (Carr, 1996), but this may not be optimal for all types of scanning motions.

2.5. Radial basis function interpolation—theory

It is perhaps intuitively obvious to attempt a traditional functional interpolation method for the reconstruction problem. In other words, choose a particular function (such as a polynomial), determine the polynomial coefficients to make it pass through the pixel values, then evaluate at regular intervals to produce a voxel array. There have been no previously published attempts at functional interpolation of 3-D freehand ultrasound data, since there are severe computational demands to overcome. For example, simple volume splines (Nielson, 1993) require solving a set of N linear equations, where N is the number of pixels summed over all B-scans. This requires $O(N^3)$ calculations. For modern computer workstations, N cannot be much larger than 500 before this becomes prohibitively slow and numerical inaccuracies arise (Nielson, 1993). This makes a typical ultrasound reconstruction problem of several million pixels infeasible.

There is a great deal of literature on interpolation, spanning a variety of disciplines, and progress has recently been made in the area of tackling very large data sets. Two good reviews are found in Franke (1982) and Nielson (1993). In order to select an appropriate method for solving the 3-D ultrasound reconstruction problem, a list of requirements is listed below:

- the method must interpolate scattered trivariate data;
- the method must have low complexity, i.e. $O(N)$, and preferably be non-iterative;
- the interpolating function must be smooth;
- both interpolation and approximation must be possible;
- large overshoots should ideally be avoided.

The smoothness requirement arises from an assumption that the input data (the set of B-scans) is smooth at a scale of several B-scan pixels. This assumption can be tested against knowledge of the acquisition process. While the underlying anatomy is not smooth at this scale, it is measured by a finite width ultrasound beam with a smooth intensity profile. This is tantamount to convolution of the anatomical function with the beam profile. Close inspection of any ultrasound image reveals that anatomical boundaries are displayed as somewhat blurred edges, several pixels wide. This applies to speckle too. It is therefore reasonable to specify a smooth function to interpolate this data.

The approximation requirement arises from the existence of measurement errors. These errors include tissue motion (such as breathing, pulsative and whole-body motions), position sensor errors and calibration errors. This means that we want to be able to change the interpolating function into an approximating function that passes close to, but not exactly through, the data points. Interpolation should be the default only if the data are perfect.

The final requirement of eliminating overshoots relates to the desire to have the range of interpolated voxel values in the same [0, 255] grey-level range as the B-scans. This requirement is related to the approximation requirement, since an approximating function can often reduce overshoots compared to interpolating functions.

After surveying the recent advancements in trivariate interpolation of large data sets, we discovered a method ideally suited to our requirements. This method was developed recently by researchers at the University of Illinois for interpolation of multivariate geographical data sets^c (Mitášová *et al.*, 1995). They dubbed the method ‘completely regularized splines with tension’. The Illinois method is summarized as follows.

Consider a set of pixel values $p_j, j = 1, \dots, N$ that are located at the positions \mathbf{x}_j , where $\mathbf{x}_j = (x_j, y_j, z_j)$ is expressed with respect to the voxel array. The basic idea is to find a spline $S(\mathbf{x})$ that passes as closely as possible to the data points and is as smooth as possible. These two requirements can be combined together such that we find the $S(\mathbf{x})$ that

^cSee also <http://www.cecer.army.mil/grass/viz/VIZ.html>

fulfils

$$\sum_{j=1}^N |p_j - S(\mathbf{x}_j)|^2 + wI(S) = \text{minimum.} \quad (1)$$

The first component is the deviation of the spline from the data points and the second is a smoothness function $I(S)$ which penalizes non-zero partial derivatives of $S(\mathbf{x})$. The weight w determines the relative cost of the two components. For a d -dimensional spline, $I(S)$ is a smooth seminorm given by (Mitášová and Mitáš, 1993)

$$I^2(S) = \sum_{\alpha} B_{\alpha} \int \dots \int_{\mathcal{R}^d} \left[\frac{\partial^{|\alpha|}}{\partial x_1^{\alpha_1} \dots \partial x_d^{\alpha_d}} S(\mathbf{x}) \right]^2 dx_1 \dots dx_d \quad (2)$$

where $\alpha = (\alpha_1, \alpha_2 \dots \alpha_d)$ is a multi-index with non-negative integer components, with

$$|\alpha| = \sum_i \alpha_i$$

and $\{B_{\alpha}\}$ are some non-negative constants. The solution to Equation (1) can be expressed as

$$S(\mathbf{x}) = T(\mathbf{x}) + \sum_{j=1}^N a_j \mathbf{R}(\mathbf{x}, \mathbf{x}_j) \quad (3)$$

where $T(\mathbf{x})$ is the trend function and $\mathbf{R}(\mathbf{x}, \mathbf{x}_j)$ is a radial basis function (RBF) whose form depends on the choice of $I(S)$ (Talmi and Gilat, 1977).

For the 2-D case, if $I(S)$ is chosen to minimize the cost of the second (partial) derivatives only, then the familiar thin-plate spline results. If the same $I(S)$ is used for the 3-D case, the first derivatives of the RBF are divergent at the data points (Mitáš and Mitášová, 1988): this would cause severe difficulties should we wish to estimate 3-D image gradients directly from the RBFs. By carefully choosing a particular set of weights $\{B_{\alpha}\}$, it is possible to obtain a simple analytic expression for an RBF with regular derivatives of all orders everywhere (Mitášová and Mitáš, 1993). This choice results in $T(\mathbf{x}) = a_0$, a constant, and

$$\mathbf{R}(\mathbf{x}, \mathbf{x}_j) = \frac{\phi^3}{4\pi} \left[\frac{1}{\phi r} \text{erf}\left(\frac{1}{2}\phi r\right) - \frac{1}{\sqrt{\pi}} \right] \quad (4)$$

where $r = |\mathbf{x} - \mathbf{x}_j|$ is the distance from \mathbf{x} to \mathbf{x}_j , and erf is the error function (Abramowitz and Stegun, 1965). The parameter ϕ is a generalized tension parameter, and it controls the distance over which the point influences the resulting hypersurface. The multiplicative constant $\phi^3/4\pi$ can be omitted, since it can be combined with the coefficients a_j . A plot of the RBF is shown in Figure 3.^d

^dDepending on the functional to be minimized, different RBFs can be derived; see Girosi *et al.* (1993) for a review of some of these functions. It is also possible to design RBFs which do not derive from a functional.

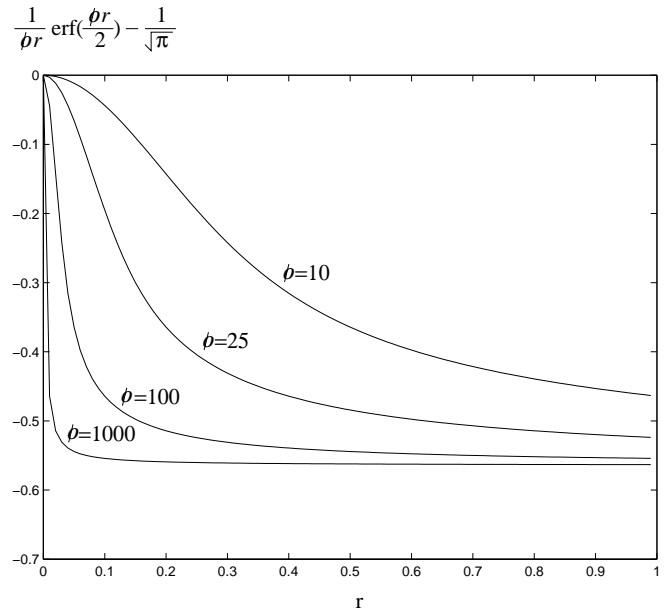


Figure 3. Radial basis function. Increasing the tension reduces the range of influence of the RBF.

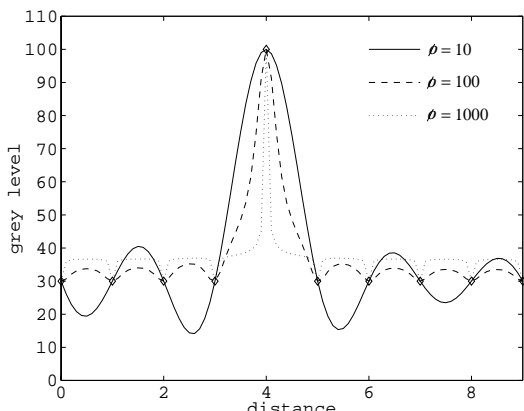
The spline coefficients can then be found by solving the set of linear equations

$$a_0 + \sum_{j=1}^N a_j [\mathbf{R}(\mathbf{x}, \mathbf{x}_j) + \delta_{ij} w] = p_i \quad (5)$$

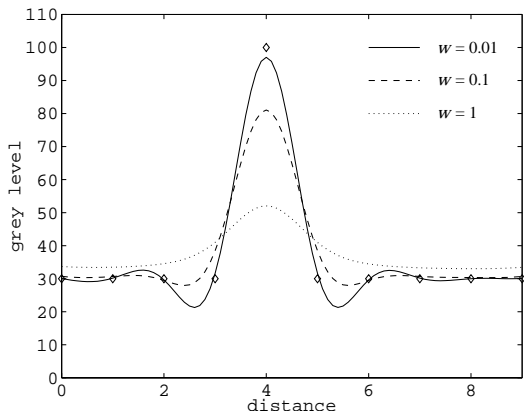
$$\sum_{j=1}^N a_j = 0 \quad (6)$$

where δ_{ij} is the Kronecker delta function.

There are therefore two parameters which can be adjusted to tune the nature of the interpolant: ϕ controls the tension and w controls the level of approximation. The goal of tuning the interpolant is to find the optimal balance between the requirements of obtaining small deviations from the data points and avoiding overshoots. As Figure 4a shows, a high level of tension limits the distance at which each point influences the overall interpolant. Yet the RBF appears spiky and does not replicate the overall shape of the data. Low tension results in overshoot. Figure 4b shows that the overshoot from low-tension interpolation may be effectively controlled by allowing a small amount of approximation. In fact, it will be shown that the combination of low tension and a small level of approximation works well with ultrasound data.



(a) Interpolation



(b) Approximation

Figure 4. One-dimensional RBF interpolation and approximation. Ten sample data points obtained from an impulse function are shown as diamonds. In (a) w is set to zero so the RBF passes exactly through the data points. The average of the data points sets the trend part of the interpolant to a value of 37. With high tension, the interpolation quickly returns to the trend between data points. With low tension, overshoots appear. Increasing the tension can be thought of as changing the nature of the interpolant from a stiff plate to a membrane. In (b) the tension level ϕ was set to a value of 20. Increasing the level of approximation reduces the amount of overshoot but can result in large deviations from the data points. A small level of approximation produces a reasonable trade-off.

2.6. Radial basis function interpolation—implementation

As previously mentioned, the RBF interpolant cannot be calculated using all the data points of an ultrasound examination

at once. In order to localize the volume splines, the scattered input data must be divided into manageable segments. The basic idea is that the interpolating function in a local region is not influenced by data at some sufficiently distant point. The voxel array is therefore divided into many small, non-overlapping rectangular segments. Individual interpolating functions are then calculated for each segment until all of the voxel array is covered. Assuming fixed-size segments, the resulting algorithm has $O(N)$ complexity.

In order to get smooth connections among the RBFs of neighbouring segments, overlapping windows are used. This means that a window is established around each segment under consideration such that it encompasses not only all the data points in the segment but also a sufficient number of neighbouring data points. All data points in the window are then used to calculate the RBF for that segment. Provided the overlap region contains sufficient data points, the RBF for each segment will closely (but not necessarily exactly) match its neighbours' RBFs: any discontinuities should be invisible in the reconstructed voxel array.

Segments of fixed size, each containing fewer than a maximum set number of data points (K_{\max}), were proposed by Mitášová and Mitáš (1993). Windows were expanded from $3 \times 3 \times 3$ surrounding segments to $5 \times 5 \times 5$ and so on, until a sufficient number (K_{\min}) of neighbouring points were included. In later work, the segmentation method was developed using an oct-tree representation of the voxel array to improve the ability to interpolate data with a heterogeneous spatial distribution (Mitášová *et al.*, 1995). This means that the segments were continuously divided into eight subsegments until each contained no more than K_{\max} points. In this way, segments of variable size were created to account for the clustering of data points. The window around each segment expanded equally in all directions until it encompassed at least K_{\min} points.

If the data are only mildly heterogeneous, this windowing method works well. However, the problem of 3-D ultrasound reconstruction involves highly clustered data; all of the input data lie within the planes of the B-scans. For this reason, we have developed a more flexible windowing method.

The basic problem with expanding a window until a fixed number of data points are encompassed, is that all the data points may lie on only one side of the segment. This can create problems with continuity of the interpolating function between segments. We propose to expand the window around the segment until data points are found in all directions around the segment. Examples of the conventional and improved windowing methods are shown in Figure 5.

In the 3-D case, the window is expanded in all directions at first, but each of the six faces of the window stops expanding only when a sufficient number of data points fall within the

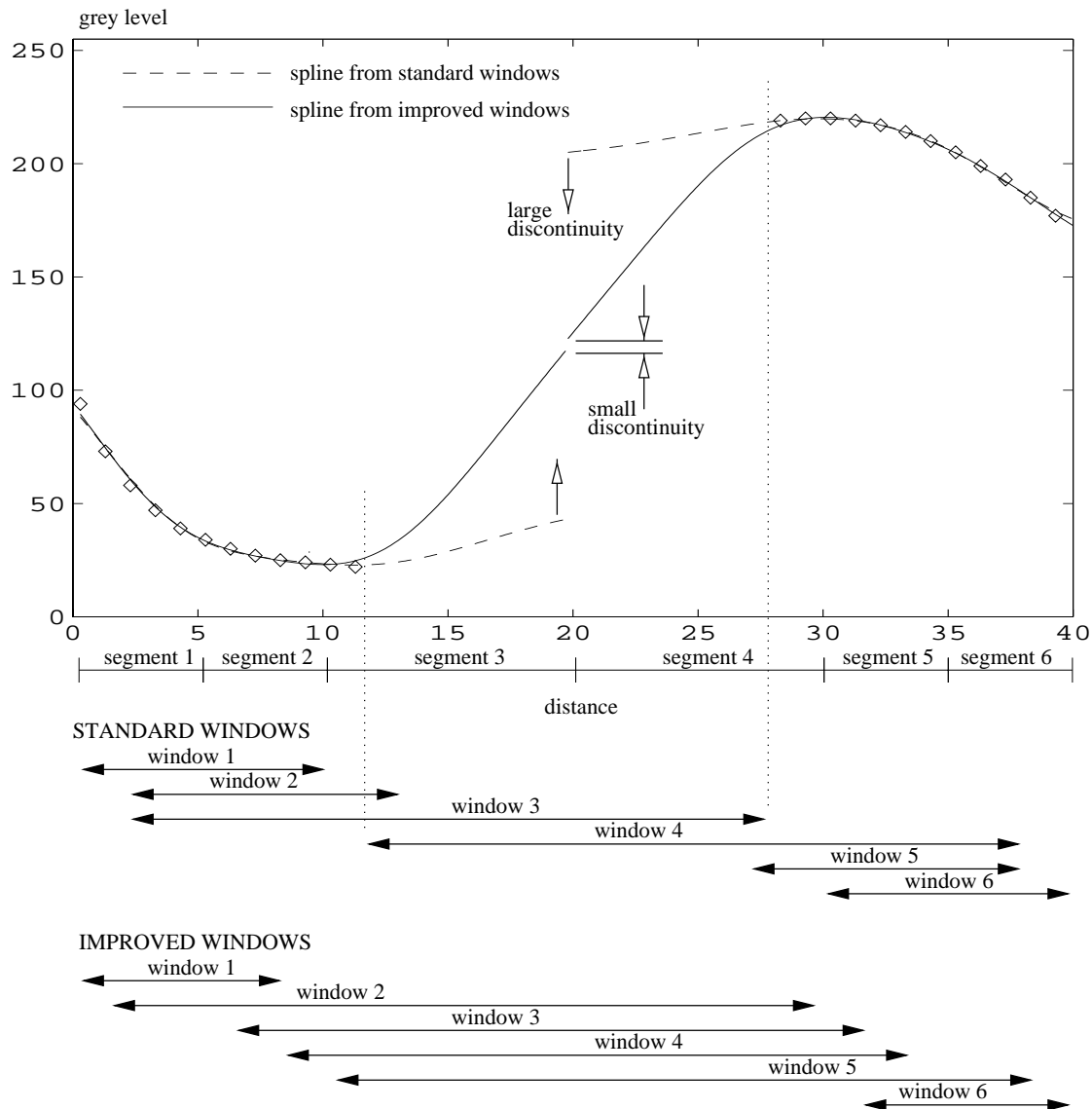


Figure 5. Example of improved windowing method. This contrived 1-D example illustrates the potential problem of the standard windowing method. Segments are created by subdividing the length of interest into a binary-tree so that each segment contains no more than five (K_{\max}) data points. The RBFs are calculated (with tension $\phi = 3$, and smoothing $w = 0.01$) for each segment using the data that falls within the surrounding window. The standard windowing method expands in both directions from the segment in single increments until 10 (K_{\min}) data points in total are obtained. The standard windows 3 and 4 only contain data on one side of the segment. This creates a large discontinuity in the interpolating function between segments 3 and 4. The new windowing method expands in both directions until at least 4 points are found on each side of the segment, or the limits of the data set are encountered. In this way, the interpolants for segments 3 and 4 contain data from both sides of the segments and therefore meet much closer together.

region defined by that direction (see Figure 6). In practice, expansion of the window in a given direction also stops when it reaches the extents of the voxel array. Testing which region a data point lies in is a potentially time-consuming operation.

We perform this test efficiently by examining the sign of the residual when the point's coordinates are substituted into the homogeneous equations of the various planes separating the regions.

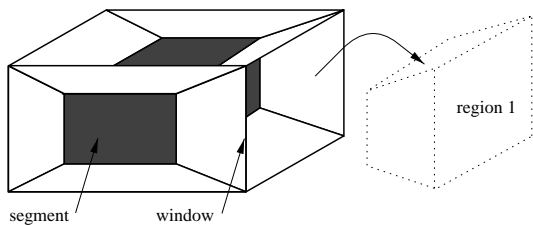


Figure 6. Segment and surrounding window. The segment is the shaded volume surrounded by the window. The window must encompass data points in each of the six regions around the segment, one of which is highlighted. This is done by expanding each of the six faces of the window until each region contains a minimum number of data points. Determination of which region a point falls into is calculated efficiently using the cross products of the vectors to the corners of the planes separating the regions.

The Illinois software was designed to work with 1000–10 000 data points, so a number of practical changes were made. In order to accommodate several million data points from an ultrasound examination, points in the oct-tree are stored using recursive dynamic memory allocation. In this way, no memory is wastefully allocated for empty segments. We also designed the oct-tree segmentation to allow segments to be divided into four (quad-tree) or two (binary-tree) subsegments when one dimension of the segment is only 1 voxel wide. This improves the ability to divide the volume into manageable segments. However, some very large segments can remain. For example, a single empty segment between two nearly parallel B-scans can extend occasionally the full length and width of the B-scans. The window around this segment, expanding one voxel at a time, will suddenly encompass an entire neighbouring B-scan in a single step. This produces an intractable number of data points, so we also choose to chop these large, empty segments into smaller segments.

In summary, we have a localized trivariate spline with $O(N)$ complexity. The method is efficient enough to handle very large data sets and flexible enough to handle highly heterogeneous data. The smooth interpolating function has regular derivatives of all orders, and has good accuracy compared with other interpolation methods (Mitášová and Mitáš, 1993). It also has a variable tension and can be tuned between interpolation and approximation.

3. COMPARISONS

3.1. Apparatus

The freehand acquisition system comprises an ultrasound scanner, a position sensor and a computer for data acquisition. A Toshiba Powervision 7000 scanner (Toshiba America Medical Systems, Tustin, CA) was used with a

Polhemus FASTRAK magnetic position sensor (Polhemus Incorporated, Colchester, VT) mounted on the probe. Calibration to determine the location of the position sensor with respect to the probe was performed using the Cambridge phantom (Prager *et al.*, 1998a). The Stradx acquisition software (Prager *et al.*, 1999) was used in conjunction with an 8-bit framegrabber and a Silicon Graphics Indy workstation (Silicon Graphics Incorporated, Mountain View, CA). The images were matched to the position sensor readings and recorded at a rate of 25 frames/s.

3.2. *In vivo* examinations

Two *in vivo* examinations were performed on a healthy human subject. First, an examination of a thyroid gland was performed with a 7 MHz linear array probe. A depth setting of 40 mm was used giving a resolution of 0.087 mm/pixel. Each B-scan was cropped to 328×409 pixels. A single sweep of the organ with a slow and steady motion resulted in a dense set of 219 nearly parallel B-scans. Figure 7 shows the outlines of the set of B-scans and a typical B-scan.

The second examination was performed with a fan-shaped sweep over the extents of the bladder. A 3.75 MHz convex curvilinear array probe was used with a depth setting of 140 mm, giving a resolution of 0.34 mm/pixel. Because the probe produces sector-shaped B-scans, the acquired 480×413 pixel images were masked so that only the ultrasound intensity data were used in each of the interpolation methods. Figure 8 shows the outlines of the set of B-scans and a typical B-scan.

These two examinations were chosen because they allow tests of the reconstruction methods with different organs, probes, depth settings, ultrasound machine settings and types of probe motion.

3.3. Tests

The tests are designed to evaluate the ability of the reconstruction methods to interpolate the ultrasound data and fill in gaps on a plane. This is essentially what is required for the principal application, which is reslicing of the voxel array. Reslicing is routinely used for visualization as well as quantitative data analysis; for example, segmentation contours are often defined on reslice planes prior to volume estimation or surface rendering.

Since the true underlying anatomical function is unknown, we have decided to test the different methods by artificially removing data from the two examinations. The four different reconstruction methods are then evaluated on their ability to predict the intensity values at the locations where the data were removed. In other words, a good reconstruction method will interpolate the removed data points with values very near to the data that was originally there.

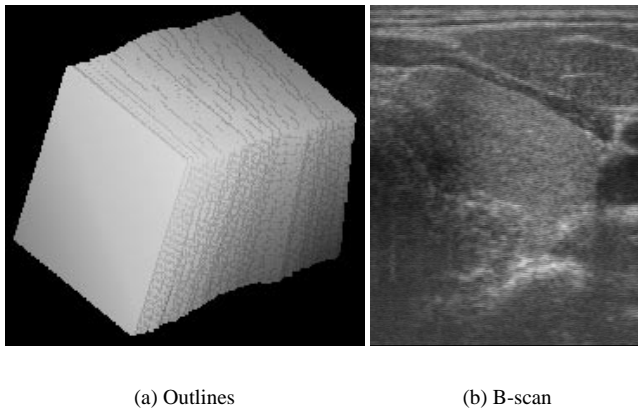


Figure 7. Thyroid examination. The outlines of the B-scans are shown in (a) with a typical B-scan shown in (b).

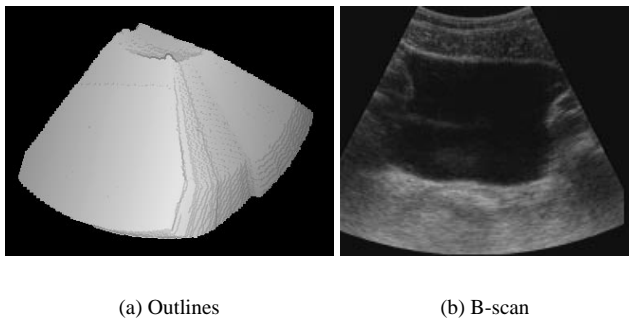


Figure 8. Bladder examination. The outlines of the B-scans are shown in (a) with a typical B-scan shown in (b).

First, a B-scan near the middle of the sweep is selected. The voxel array (with voxels equal in size to the pixels) is aligned exactly with this B-scan such that pixels fall exactly onto voxels. A percentage of the pixels are then removed randomly from the B-scan, creating gaps of various sizes. The rest of the pixels and all other B-scans in the reconstruction are used in the interpolation to fill in all voxels in the voxel array. The values of the removed (original) pixels can now be compared with the values of the voxels aligned with them. The voxel array stores the interpolation results as floating point numbers to avoid the influence of quantization. The average of the difference between the interpolated and the original data over all missing data points is calculated by

$$V = \frac{1}{M} \sum_{i=1}^M |p_i - v_i| \quad (7)$$

where p_i is the original pixel that was removed from the

reconstruction, v_i is the interpolated value of the voxel aligned with p_i and M is the number of removed pixels. A low value of V indicates a good ability to interpolate over the gaps.

The tests are performed with eight different percentages of removed data: 0%, 25%, 50%, 75%, 100%, 300%, 500% and 700%. For the 25%, 50%, 75% and 100% tests, pixels are removed only from the selected B-scan n . The 300% test refers to removing all of the pixels of B-scan n and all of B-scans $n - 1$ and $n + 1$. The 500% and 700% tests further remove B-scans $n \pm 2$ and $n \pm 3$ respectively. The 0% test is also included, since a reconstruction method may not exactly replicate the original data points. For example, a functional approximation method will miss the data points. For the 0% test alone, V is calculated over all pixels of the selected B-scan.

Each of the eight tests are repeated for 10 different B-scans to give mean and variance estimates of V . In this way, 80 voxel arrays are created for each of the four reconstruction methods, producing 320 voxel arrays in total. A further 320 voxel arrays are created in the same way for the bladder examination.

3.4. Reconstruction methods

The VNN interpolation method is implemented by traversing the voxel array and filling each voxel with the value of the nearest pixel. The PNN interpolation method is implemented in two steps. The first step assigns each pixel to the nearest voxel in the array. Multiple contributions to a single voxel are averaged together. The second step fills the remaining gaps. Empty voxels are filled by taking the average of the filled voxels in a $3 \times 3 \times 3$ neighbourhood. The remaining unfilled voxels are then filled by averaging originally filled voxels in a $5 \times 5 \times 5$ neighbourhood and so on, until all voxels are filled. This is similar to the method described in Nelson and Pretorius (1997).

The reported high-quality reconstructions described in Barry *et al.* (1997) led us to choose the inverse DW method with a spherically shaped local neighbourhood. The one parameter to choose in this method is the radius, R , of the neighbourhood. If R is set to cover the largest gaps in the 700% tests, it would be much too large for the tests with smaller gaps and excessive smoothing would occur. R must be set to reasonable but not arbitrary values for each of the tests.

In Barry *et al.* (1997), a 7 MHz linear array probe was used to examine the carotid artery, a similar examination to the thyroid gland. Two R values were suggested: 0.25 and 0.5 mm. In our examination of the thyroid gland, the distances between the centres of the B-scans range from 0.09 to 0.52 mm, with a mean of 0.32 mm. Using a neighbourhood

of radius R equal to 0.25 mm is therefore not large enough to fill in all gaps, so 0.5 mm is used in the 0%, 25%, 50%, 75% and 100% tests.^e For the 300%, 500% and 700% tests, R must be increased to cover all gaps. We chose to increase R by the mean (0.32 mm) of the B-scan spacing. This means R was set to 0.82 mm (0.5 mm + 0.32 mm), 1.14 mm (0.5 mm + 2 × 0.32 mm) and 1.46 mm (0.5 mm + 3 × 0.32 mm) for the 300%, 500% and 700% tests respectively.

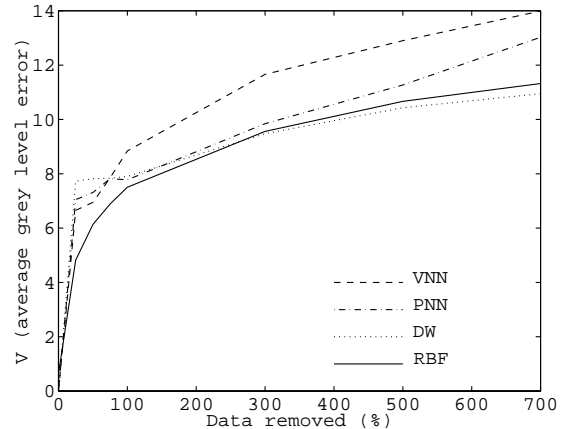
To be consistent, the values of R for the bladder reconstruction are set in a similar fashion. R is set to the maximum distance between B-scans for the 0%, 25%, 50%, 75% and 100% tests, and then increased by the mean distance between B-scans for the 300%, 500% and 700% tests. Since the examination used a fan-shaped sweep, the B-scan spacing is measured at the bottom centre of the B-scan, where the gaps are larger. The B-scan spacing ranges from 0.41 to 0.80 mm, with a mean of 0.60 mm. The value of R is therefore set to 0.80 mm for the 0%, 25%, 50%, 75% and 100% tests, and 1.40 mm (0.80 mm + 0.60 mm), 2.00 mm (0.80 mm + 2 × 0.60 mm) and 2.60 mm (0.80 mm + 3 × 0.60 mm) for the 300%, 500% and 700% tests respectively.

The RBF method is implemented using the oct-tree segmentation and improved windowing technique described in Subsection 2.6. K_{\max} is set to 30 data points, and each region of the window is required to contain at least 5 data points.

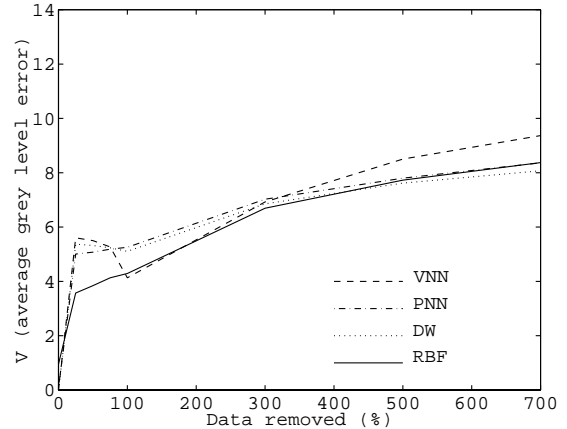
For the 300%, 500% and 700% tests of the thyroid examination, large gaps and extremely long computation times result. The window is therefore expanded faster in the two directions perpendicular to the selected B-scan (towards the neighbouring B-scans) than in the four directions in the plane of the B-scan. This avoids making the window too large and enveloping an intractable number of data points. We do this simply to speed up the calculations, since such a large overlap is not required to get smooth transitions among the segments. As a reassurance, at least 20 points per region are required for these 300%, 500% and 700% tests, compared to the minimum of 5 points per region for all other tests.

The tension and approximation parameters are tuned manually by testing V for a randomly selected B-scan. A fairly low tension ϕ combined with a small amount of data smoothing w results in a good trade-off between minimizing overshoot and passing very near the data points. This, in turn, produces a small value of V . For the thyroid examination, we set $\phi = 17$ and $w = 0.01$. The bladder examination uses $\phi = 25$ and $w = 0.1$. These values fall within the range of values

^eIt appears that setting R to half of the maximum centre distance between B-scans would fill the entire volume without gaps. But because the scan planes are not exactly parallel, larger gaps than 0.52 mm exist. In fact, the value of 0.5 mm is just sufficient to cover all gaps.



(a) Thyroid



(b) Bladder

Figure 9. Average grey-level error for the thyroid and bladder data sets. For each of the four reconstruction methods, V is calculated for various percentages of removed data.

typically used for geographic data interpolation (Mitášová *et al.*, 1995).

4. RESULTS

The overall trends of the test results are illustrated in Figure 9 and tabulated in Tables 1 and 2. To give an indication of the distributions of V over the 10 trials, box-and-whisker plots are shown in Figures 10 and 11. A small but representative set of images of the interpolated data are shown in Figures 12–15.

Table 1. Interpolation error V for the thyroid examination. μ is the mean of V and σ is the standard deviation

	VNN		PNN		DW		RBF	
	μ	σ	μ	σ	μ	σ	μ	σ
0%	0.00 ¹	0.00	0.00 ¹	0.00	0.00 ¹	0.00	0.64	0.03
25%	6.65 ²	0.12	7.05 ²	0.12	7.73 ²	0.27	4.82	0.25
50%	6.95 ²	0.14	7.31 ²	0.13	7.82 ²	0.30	6.14	0.33
75%	7.86 ²	0.16	7.82 ²	0.13	7.84 ²	0.35	6.89	0.39
100%	8.84	2.60	7.78 ²	0.64	7.90	0.42	7.51	0.78
300%	11.66 ²	2.00	9.85	0.75	9.48	0.47	9.56	0.34
500%	12.90 ²	1.65	11.27 ²	0.73	10.43	0.53	10.67	0.29
700%	13.99 ²	1.32	13.03 ²	1.00	10.95 ¹	0.52	11.32	0.23

¹The assertion $\mu < \mu_{\text{RBF}}$ is statistically significant for a confidence level of 0.05.
The assertions are tested with the paired-sample t-test statistical method (Hogg and Ledolter, 1987).

²The assertion $\mu > \mu_{\text{RBF}}$ is statistically significant for a confidence level of 0.05.

Table 2. Interpolation error V for the bladder examination. See the caption of Table 1 for an explanation of the tabulated terms and symbols

	VNN		PNN		DW		RBF	
	μ	σ	μ	σ	μ	σ	μ	σ
0%	0.00 ¹	0.00	0.00 ¹	0.00	0.00 ¹	0.00	0.96	0.03
25%	5.60 ²	0.39	5.01 ²	0.22	5.37 ²	0.09	3.57	0.25
50%	5.50 ²	0.40	5.08 ²	0.25	5.32 ²	0.09	3.85	0.31
75%	5.27 ²	0.50	5.19 ²	0.35	5.24 ²	0.10	4.13	0.40
100%	4.13	0.38	5.25 ²	0.40	5.11 ²	0.14	4.29	0.37
300%	6.92	0.40	7.03 ²	0.15	6.85 ²	0.12	6.69	0.19
500%	8.50 ²	0.23	7.80 ²	0.14	7.62 ¹	0.11	7.73	0.16
700%	9.37 ²	0.26	8.36	0.18	8.07 ¹	0.09	8.37	0.16

4.1. VNN interpolation

For both examinations, V is zero at 0% data removal, since the voxels are set to their nearest neighbours: the original pixels of the B-scan. At 25%, 50% and 75%, the nearest neighbours of the voxels are mainly the remaining pixels of the selected B-scan. Therefore, the resulting interpolated images appear as a patchwork of irregularly shaped pieces and relatively large values of V result.

For the 100–700% tests, the interpolated image is made from the projection of the pixels from the nearest B-scan, so the patchwork appearance disappears. For the thyroid examination, the variance of V is large because some of the projections of neighbouring B-scans closely match the original B-scan, but others do not. This depends on both the level of registration error and the similarity of the pixel values. The values of V are generally greater than the other three reconstruction methods.

For the bladder examination, the 100–700% tests show a smaller variance of V than the thyroid examination, but the variance is still large compared with the other methods. The mean, however, is lowest at 100%, and increases again for the higher percentage tests. This may be explained by comparing the level of registration errors to the voxel size. If registration errors, such as position sensor error, are of similar absolute magnitudes for the two examinations, the errors will have a smaller effect on the bladder tests. This is because the voxel size is larger in the bladder tests than in the thyroid tests, so the effect of the errors is reduced. Yet, as more and more B-scans are removed, the relative registration errors increase, thereby making V increase again.

In general, however, the results look sharp and detailed for the 100–700% tests, since the projected data exhibits no blurring. Moreover, the boundaries between the portions of the projected data are not discernible for any tests of either

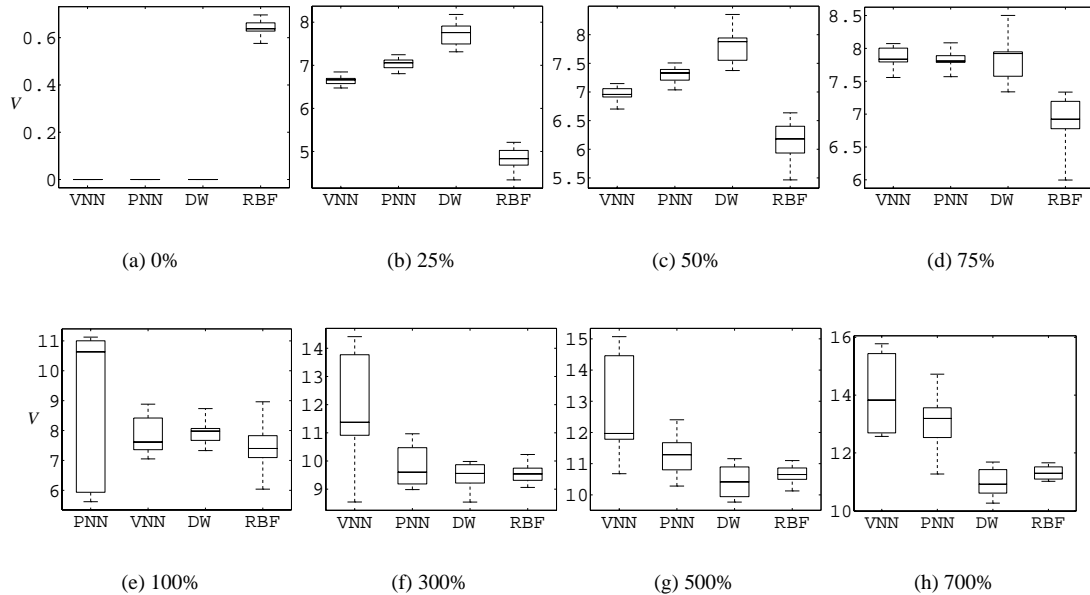


Figure 10. Interpolation error V for the thyroid examination. The box-and-whisker plots show the three quartiles and the extremes of V calculated over the 10 trials at each percentage of removed data. The median (50th percentile) is the line inside the box of the 25th and 75th percentiles of V . The whiskers show the minimum and maximum values.

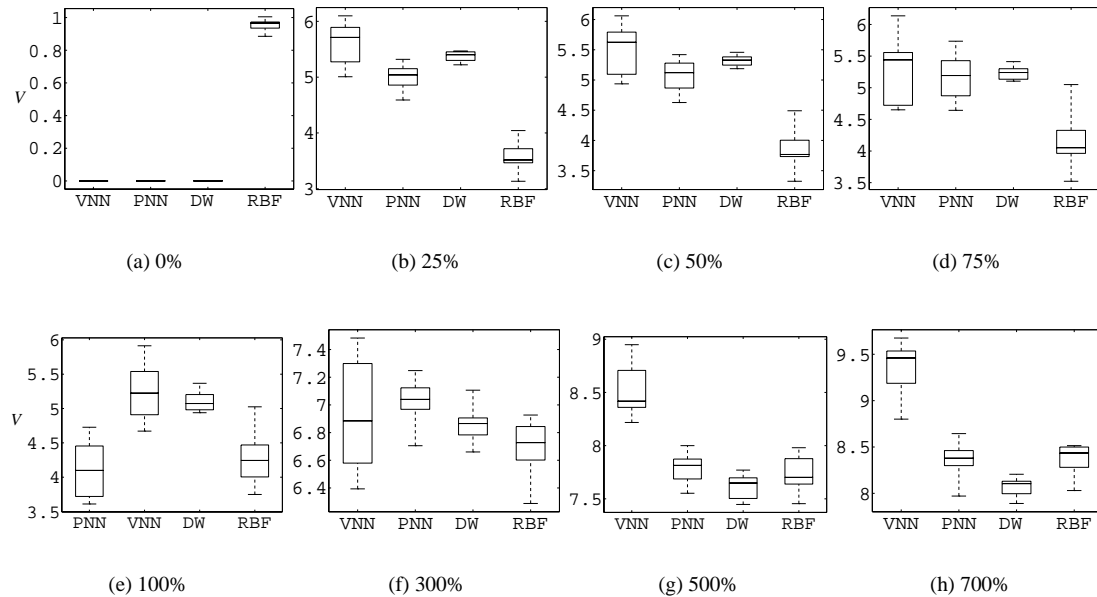


Figure 11. Interpolation error V for the bladder examination. See the caption of Figure 10 for an explanation of the box-and-whisker plots.

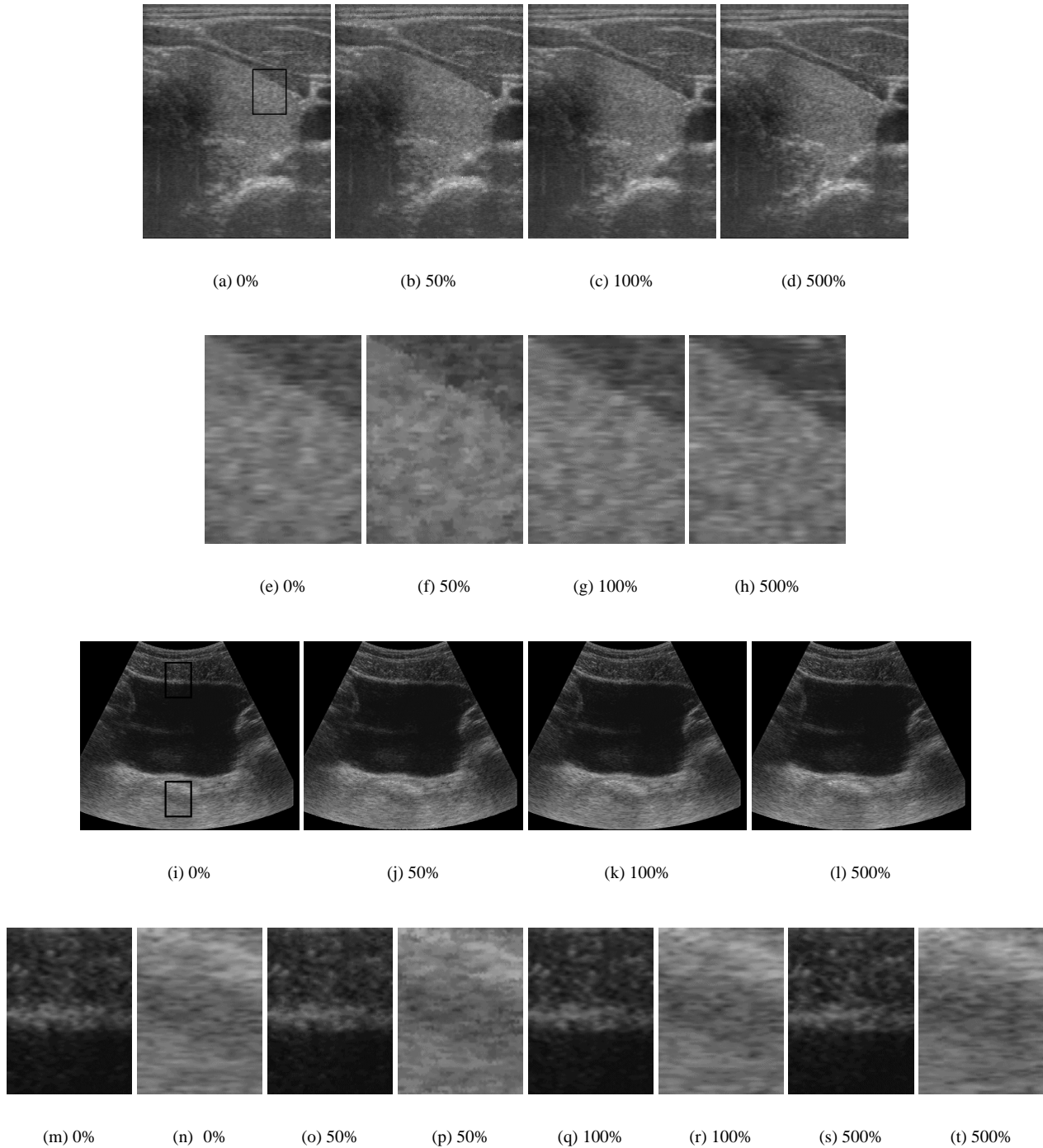


Figure 12. Typical B-scans interpolated by the VNN method. All images are shown for a particular B-scan with various percentages of data removed. Images (a)–(d) are from the thyroid examination, with expanded views of the area indicated in image (a) shown in images (e)–(h). Images (i)–(l) are from the bladder examination, with expanded images of the top and bottom areas indicated in image (i) shown in images (m)–(t). See also the accompanying CD-ROM for larger versions of these images.

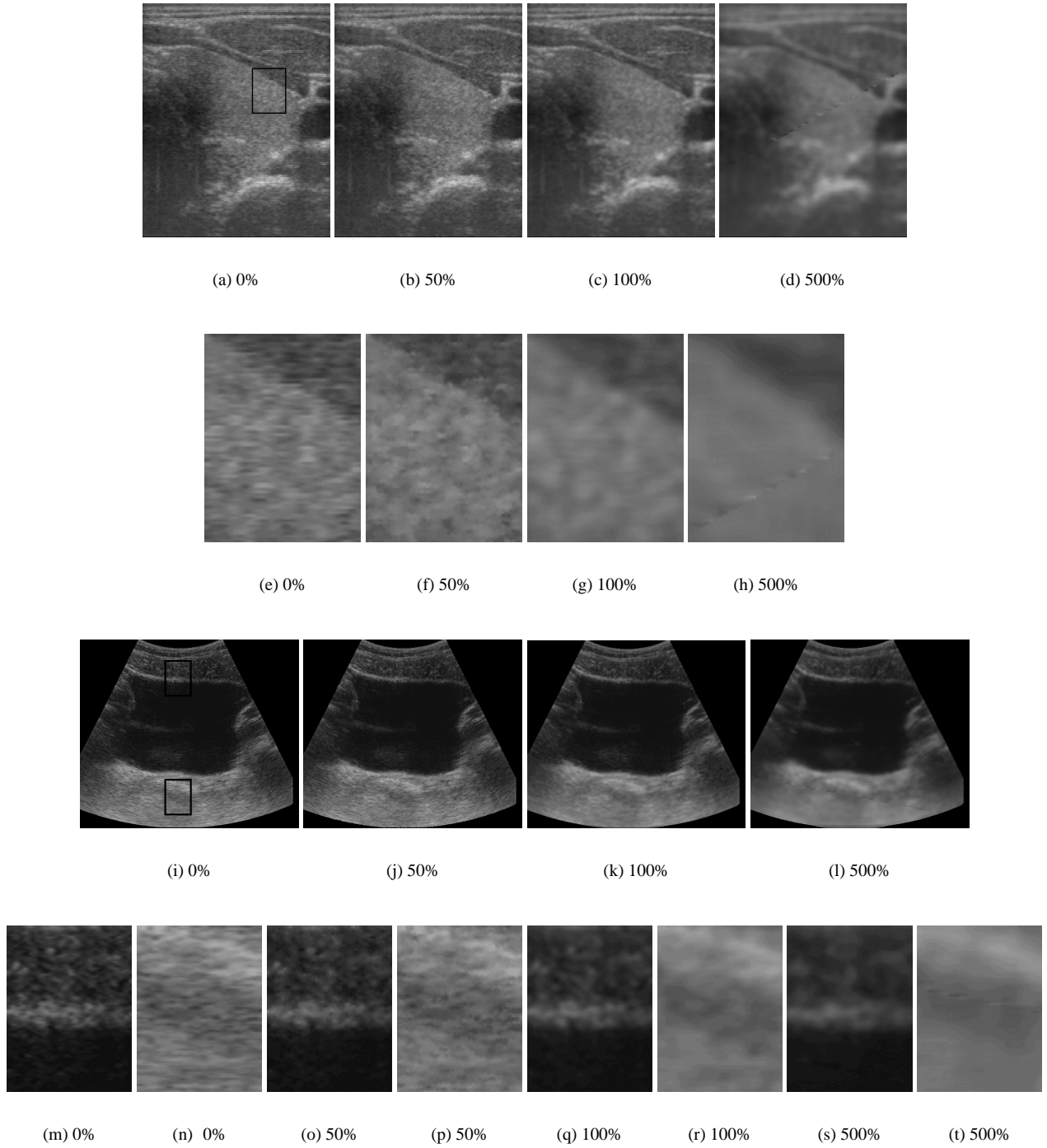


Figure 13. Typical B-scans interpolated by the PNN method. See the caption of Figure 12 for an explanation of the images.

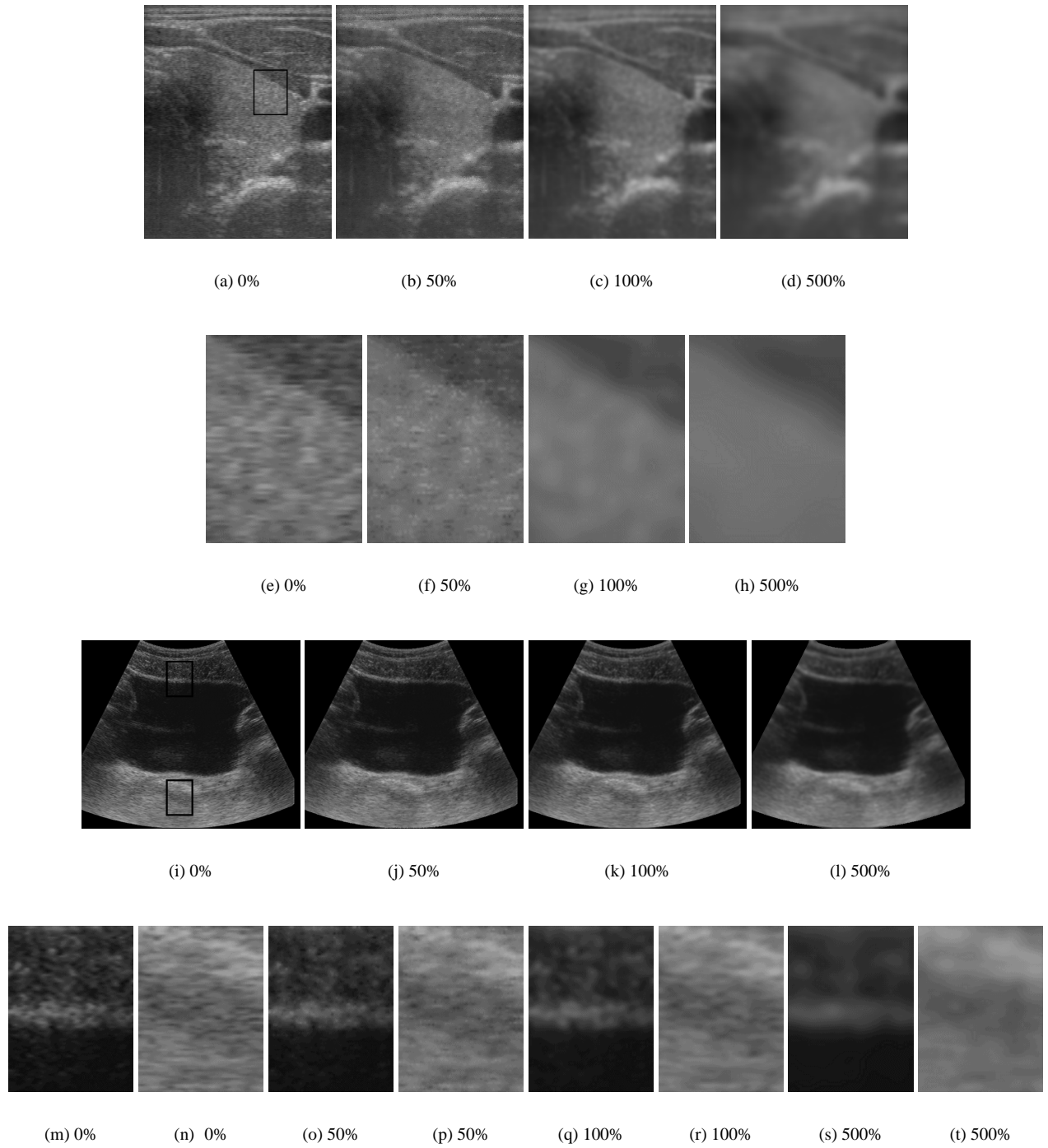


Figure 14. Typical B-scans interpolated by the DW method. See the caption of Figure 12 for an explanation of the images.

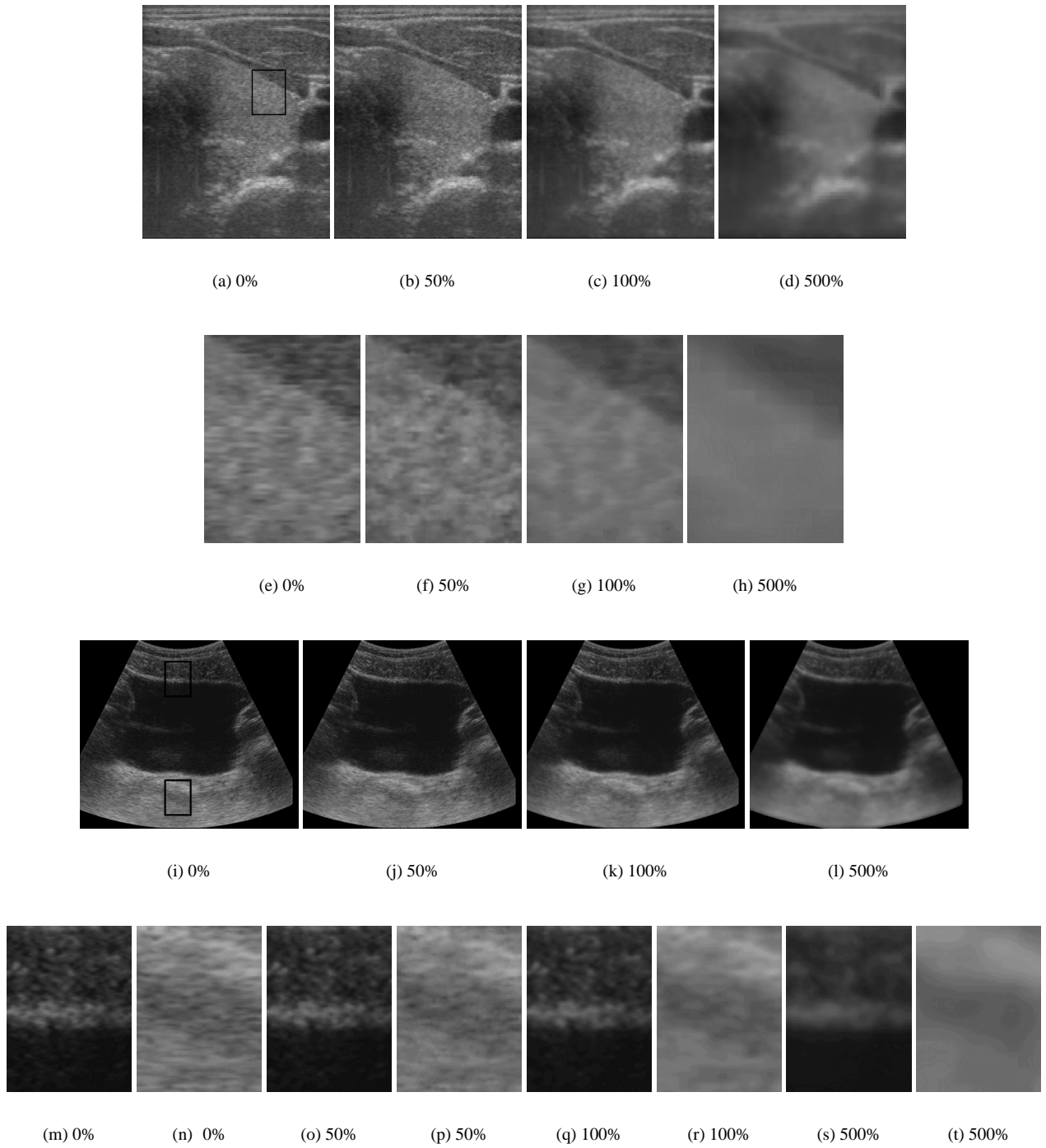


Figure 15. Typical B-scans interpolated by the RBF method. See the caption of Figure 12 for an explanation of the images.

examination. This suggests that the registration errors are mainly small and the images vary slowly from one B-scan to the next.

4.2. PNN interpolation

For both examinations, V is zero at 0% data removal, since the nearest neighbours to the voxels are the original pixels. At 25%, 50% and 75%, the gaps are filled mainly with an average of the remaining pixels in the original B-scan. The interpolated image appears as a patchwork again, and relatively large values of V result.

For the thyroid examination, the mean of V increases progressively for the 500% and 700% tests compared with the relatively good performance in the bladder examination. This can be explained by noticing that the gaps in the bladder data set are much smaller at the top than the bottom, which limits the blurring effect of the ‘hole-filling’ stage to the large gaps at the bottom of the bladder images. With lower amounts of blurring in the bladder tests, lower values of V result.

Unfortunately, the images exhibit significant reconstruction artefacts for both examinations, especially for the 500% and 700% tests (see especially Figure 13d and h). A visible boundary exists between portions which are filled, for example, by averages of a $7 \times 7 \times 7$ neighbourhood, and portions filled by a neighbourhood of $9 \times 9 \times 9$, because they involve different amounts of smoothing. The boundaries between the voxels filled by the first ‘bin-fill’ stage and second ‘hole-fill’ stage are also visible.

4.3. DW interpolation

For both examinations, V is zero for the 0% tests, since the weights on the original pixels that fall exactly on the voxels approach infinity. At 25%, 50% and 75%, the images can be considered as the superposition of two effects. The first effect arises from the voxels filled by the original data weighted by infinity. The second effect arises from the voxels in the gaps that are calculated from a weighted average of many neighbouring pixels. The resulting interpolated data are therefore a combination of the remaining pixels from the original B-scan and smoothed data in the gaps.

Since the radius R of the neighbourhood is tailored for each test of 100% and above (as explained in Subsection 3.4), the values of V for the thyroid examination are relatively small. However, for the 100% test on the bladder examination, the mean of V is considerably higher than the RBF method. This is because R is too large at the top of the image where the data are dense (but just large enough to fill the gaps at the bottom), resulting in excessive smoothing at the top. For 300–700%, the values of V improve, since the removal of data offsets the increase in R .

The images show progressive blurring as the percentage of removed data increases, but no reconstruction artefacts are generated. For the thyroid examination, the level of blurring is uniform. For the bladder examination, blurring is slightly greater near the top of the images.

4.4. RBF interpolation

For both examinations, V is greater than 0 for the 0% test, since the approximating function does not pass exactly through the original pixel values. For both examinations, however, the mean of V at 0% is <1 .

At 25%, 50% and 75%, the mean of V is considerably lower than the other methods and the resulting interpolated data appears the most detailed and least artificial. This is because the interpolation utilizes both the remaining pixel data of the original B-scan and the neighbouring B-scans. The low values of V demonstrate the ability of a functional method to use the general shape of the underlying anatomical data to interpolate across the gaps.

Yet at percentages of 100% and greater, the RBF is not always significantly better than the other methods. In particular, the VNN method matches it at 100% in the thyroid examination and at 100% and 300% in the bladder examination. The PNN method matches it at 300% in the thyroid examination and at 700% in the bladder examination. The DW method is even closer, matching the RBF method at 100%, 300% and 500% for the thyroid examination, and even slightly betters it at 700%. It also slightly betters the RBF method at 500% and 700% in the bladder examination.

One of the reasons the RBF loses some of its advantage is that the underlying shape of the anatomical data is lost when the gaps become too large. Another problem is that the RBF approaches the trend in the largest gaps. This is because the tension needs to be high enough so that no overshoots appear within the B-scan. Yet in the gaps, a higher tension results in a faster approach of the interpolating function towards the trend.

In general, however, the RBF method produces natural-looking images with no apparent artefacts. The boundaries between segments are not visible, since they are generally less significant than the grey-level quantization. No overshoots are generated either: the range of the interpolated data matches the range of grey levels in the original B-scans.

For the thyroid examination, the interpolated images become progressively blurred as the percentage of removed data increases. The level of blurring is uniform throughout the image. For the bladder examination, however, the denser data at the top of the images allows the RBF to retain a high level of detail. The blurring then progressively and smoothly increases toward the bottom of the images where the gaps

are larger. The level of blurring therefore reflects the level of uncertainty in estimation of the underlying function. In comparison, the DW method shows, counterintuitively, the greatest blurring near the top of the bladder images.

4.5. Discussion

Of the four reconstruction algorithms, the RBF technique stands out as requiring significantly more computation time than its competitors. The thyroid and bladder data sets can be reconstructed by the VNN, PNN and DW methods in a few minutes, but the RBF method requires a few hours. We should note, however, that the RBF method can be speeded up if implemented on parallel hardware. The segments can be interpolated in parallel because the memory storing the pixel values does not change (eliminating read errors). Each process also writes to a different segment in the voxel array (eliminating write errors). Since many modern ultrasound machines already have the capacity for parallel processing (the Toshiba Powervision 7000 we used for these examinations contains more than 60 Pentium processors), a practical implementation of the RBF method is not infeasible.

Looking at the graphs in Figure 9, the RBF technique would appear to be the best all-round performer. Its superiority is particularly evident with small percentages of removed data. This is because the underlying shape of the data can be used to interpolate across small gaps and reduce the effects of outliers (caused by registration errors, for instance). This is particularly evident in the bladder examination, where the data is very dense and the shape of the data readily deducible from the remaining data points. The sub-100% data removal experiments are important in the context of one of the most popular visualization techniques, any-plane slicing. Typically, the user wishes to view slices orthogonal or nearly orthogonal to the original B-scans. Thus, the slice plane is intersected by many of the B-scans and contains many true data points, as well as many gaps which need interpolating across. It appears that the RBF method performs especially well in this sort of situation.

The higher percentage tests are representative of what would happen with faster hand motion during the examination or a slower rate of acquisition by the computer. When the gaps become larger, the RBF method loses some of its advantage. The shape of the underlying data is eventually lost when the gaps become too large. Nevertheless, with few exceptions, the RBF method performs at least as well as the other methods. The performance of the RBF method can be improved by tuning the tension ϕ and smoothing w for each percentage of removed data. However, the improvements are marginal: the results are largely unchanged for tensions ϕ in the range [10, 25] and smoothing w in the range [0.01, 0.1].

Although the RBF method produces the lowest values of V , the VNN algorithm also produces very detailed images at high percentages of removed data. Since the registration errors are small, the nearest-neighbour projections appear to be seamless. Both examinations of the thyroid and bladder are of organs with a slowly varying shape, so the projections from different B-scans are similar. But if more complex shapes are scanned, or the registration errors increase, the boundaries will become more visible. Moreover, images interpolated across large gaps (which depict projections of distant B-scans) appear sharp, but are strictly incorrect since the anatomy is featured in the wrong place: the apparent high quality of the images is misleading. In contrast, the other reconstruction techniques produce progressively blurred images in regions where the data is sparse, warning the viewer that the data should be interpreted with extreme caution. Ideally, the VNN technique should be extended to communicate a confidence measure, perhaps based on the distance to the data, by colour coding.

One final point worthy of discussion is the scale of the reconstructions. Is there any point in constructing a high-resolution voxel array, with voxels having the same dimension as a pixel in the original B-scan? Three-dimensional reconstructions are susceptible to registration errors of magnitudes much larger than one B-scan pixel. The principal sources of such errors are the deformation of the anatomy due to the contact pressure of the ultrasound probe, respiratory and cardiac motion, errors in the position sensor and its calibration, along with other ultrasound-related effects, such as beam refraction (Rohling *et al.*, 1997). However, 3-D ultrasound reconstructions appear to be locally accurate. Motion artefacts show up as clear fault lines in the reconstruction volume, which are immediately apparent in any visualization:^f if they obscure the region of interest, the data can always be re-acquired. Preserving the high resolution of the B-scans in the 3-D reconstruction has significant benefits. Firstly, the speckle characteristics of slices through the reconstruction are similar to those in the original B-scans, aiding interpretation of the images by skilled ultrasonographers. Secondly, small structures can be resolved in high-resolution reconstructions but would be lost in lower-resolution reconstructions. This can sometimes make all the difference between a useful and not useful data set. For instance, Figure 16 shows a visualization of

^fThe exception is with very small, local motions, where the scale of the motion is comparable with the reconstruction resolution. In such cases, motion artefacts will not show up as spatially coherent fault lines in the reconstruction volume, and any reconstructed images should be interpreted with extreme care. However, there are very few anatomical structures which are capable of independent motion and small enough to produce such subtle artefacts: gross motion artefacts are the norm.



Figure 16. Visualization of a 16-week foetus. Image (a) shows a typical B-scan from the recorded sequence. Image (b) is a slice through a high-resolution VNN voxel array, corresponding to the diagonal white line in image (a). The slice (b) shows the foetus' right leg in profile: the vertical white line corresponds to the B-scan (a). Image (c) is a manifold visualization, which is similar to a reslice but the data are sampled from a curved surface, not a flat plane. The intersection of the surface with the reslice follows the foetus' leg, as shown by the white curve in image (b). The manifold shows a frontal view of the leg, 'unfolded' into a straight line. All five toes are visible in the manifold.

a high-resolution reconstruction of a 16-week foetus, with voxel size equal to the original B-scan pixel size. Five toes are just resolvable in the manifold view, ruling out one of the more common foetal abnormalities. Such information would not be available in a lower-resolution reconstruction. The toes were much harder to detect in the original B-scans, since the plane of the foot was virtually parallel to the mother's skin.

5. CONCLUSIONS AND FUTURE WORK

In this paper, we have developed a novel RBF reconstruction technique for freehand 3-D ultrasound, and compared it with three conventional reconstruction algorithms. In terms of reconstruction quality, the RBF method performs at least as well as the traditional reconstruction methods. It can reconstruct simultaneously areas with densely overlapping B-scans and areas with large gaps, while making a smooth transition between them. The apparent quality of the interpolated data is good, with no visible reconstruction artefacts produced in any of the tests.

The most readily apparent avenues for future work involve further development of the RBF method. For example, it would be worthwhile investigating novel implementations to improve the execution speed of the algorithm. In our current implementation, the three principal stages (identify points and windows, solve for the RBF parameters, evaluate the RBFs to fill the voxels) take roughly the same amount of time. A careful analysis of the efficiency of each stage may help determine the priority of improvements. An implementation of the RBF technique on parallel hardware, as found in many of today's modern ultrasound machines, would also be worthwhile.

Perhaps the greatest potential improvement lies with the introduction of anisotropic tension. The RBF functions are invariant to translations and rotations, but are not scale invariant (Mitášová and Mitáš, 1993). This means that a change in the scale of the dimensions is equivalent to a change in the tension parameter. By changing the scale of the three axes individually, the tension is changed for these three directions. Since the pixel data all lie in planes, and are usually separated by gaps larger than the pixel size, the tension should be high within the B-scan to avoid overshoots, and low in the direction orthogonal to the B-scans to fill the gaps between them without approaching the trend. It is also possible to introduce weights on the pixels (Mitášová *et al.*, 1995) when, for example, estimates of registration error or signal fall-out are available. Finally, the optimal combination of tension and smoothing could be found using statistical techniques such as cross-validation (Mitášová *et al.*, 1995).

Since the RBF method alone employs a functional approach, it offers a number of unique opportunities. For example, derivatives of any order can be computed directly from the interpolating function. This may be useful for visualization, registration and segmentation. The functional representation may also be useful for data compression. For lower-resolution voxel arrays, the functions can be passed directly through low-pass filters for proper anti-aliasing. Since the function usually passes further away from outliers (when a non-zero smoothing parameter is used), the regions

with high predictive error can be determined. This may be useful, for example, for investigations into registration errors.

Another avenue of future work would be to examine iterative approximation algorithms for the freehand 3-D ultrasound reconstruction problem. For example, multi-dimensional thin-plate splines under tension (Terzopoulos 1986, 1988) could be fitted to all the data globally, circumventing the windowing required to reduce the complexity of the RBF method. Moreover, it might be possible to use one of the other reconstruction methods, such as VNN, to provide an initial approximation for the iterative spline technique.

In summary, all four methods considered in this paper produce reasonable reconstructions when the gaps between data points are kept at realistic levels. It would be misleading to declare a winner based on the experiments reported here: all the methods could be improved or tailored to a particular type of examination. However, the RBF technique can be singled out as showing particular promise for the future. While its considerable computational expense might limit its use in everyday clinical environments, there are many applications which could benefit from the unique properties of a functional approach.

ACKNOWLEDGEMENTS

The original program code for the regularized splines with tension was kindly provided by Lubos Mitáš and Helena Mitášová. Lubos Mitáš is at the National Center for Supercomputing Applications at the University of Illinois. Helena Mitášová is at the Geographic Modeling Systems Laboratory at the University of Illinois. Development of the original spline code was carried out in cooperation with the United States Army Construction Engineering Research Laboratories. Thanks are due to the anonymous referees, whose constructive comments helped to improve the original version of this paper. Thanks also to Diana Galletly and Patrick Gosling for permission to publish the data in Figure 16. The freehand acquisition system was developed by Richard Prager at the University of Cambridge. Some of the 3-D renderings were produced using the 3DViewnx visualization package. The many helpful discussions with Jonathan Carr are also appreciated. Robert Rohling is supported by Churchill College and an ORS award.

REFERENCES

- Abramowitz, M. and Stegun, I. A. (1965) *Handbook of Mathematical Functions*. Wiley, New York.
- Barry, C. D., Allott, C. P., John, N. W., Mellor, P. M., Arundel, P. A., Thomson, D. S. and Waterton, J. C. (1997) Three-dimensional freehand ultrasound: image reconstruction and volume analysis. *Ultrasound Med. Biol.*, 23, 1209–1224.
- Carr, J. (1996) *Surface Reconstruction in 3D Medical Imaging*. Ph.D. Thesis, University of Canterbury, Christchurch, New Zealand.
- Fenster, A. and Downey, D. B. (1996) 3-D ultrasound imaging—a review. *IEEE Eng. Med. Biol. Mag.*, 15, 41–51.
- Fine, D., Perring, S., Herbetko, J., Hacking, C. N., Fleming, J. S. and Dewbury, K. C. (1991) Three-dimensional (3D) ultrasound imaging of the gallbladder and dilated biliary tree: reconstruction from real-time B-scans. *Brit. J. Radiol.*, 64, 1056–1057.
- Franke, R. (1982) Scattered data interpolation: tests of some methods. *Math. Comput.*, 38, 181–200.
- Girosi, F., Jones, M. and Poggio, T. (1993) Priors, stabilizers and basis functions: from regularization to radial, tensor and additive splines. *A.I. Memo No. 1430*, MIT AI Laboratory, Cambridge, MA.
- Hogg, R. V. and Ledolter, J. (1987) *Engineering Statistics*. Macmillan Publishing Company, New York.
- Hottier, F. and Collet Billon, A. (1990) 3D echography: status and perspective. In Hohne, K. H., Fuchs, H. and Pizer, S. M. (eds), *3D Imaging in Medicine: Algorithms, Systems, Applications*, pp. 21–41. Springer-Verlag, Berlin.
- McCann, H. A., Sharp, J. C., Kinter, T. M., McEwan, C. N., Barillot, C. and Greenleaf, J. F. (1988) Multidimensional ultrasonic imaging for cardiology. *Proc. IEEE*, 76, 1063–1072.
- Mitáš, L. and Mitášová, H. (1988) General variational approach to the interpolation problem. *Comput. Math. Applic.*, 16, 983–992.
- Mitášová, H. and Mitáš, L. (1993) Interpolation by regularized spline with tension: I. Theory and implementation. *Math. Geol.*, 25, 641–655.
- Mitášová, H., Mitáš, L., Brown, W. M., Gerdes, D. P., Kosinovsky, I. and Baker, T. (1995) Modelling spatially and temporally distributed phenomena: new methods and tools for GRASS GIS. *Int. J. Geog. Info. Syst.*, 9, 433–446.
- Nelson, T. R. and Pretorius, D. H. (1997) Interactive acquisition, analysis and visualization of sonographic volume data. *Int. J. Imag. Syst. Technol.*, 8, 26–37.
- Nielson, G. M. (1993) Scattered data modeling. *IEEE Comput. Graphics Appl.*, 13, 60–70.
- Ohbuchii, R., Chen, D. and Fuchs, H. (1992) Incremental volume reconstruction and rendering for 3D ultrasound imaging. In *Visualization in Biomedical Computing*, Vol. 1808, *Proc. SPIE*, pp. 312–323. SPIE Press, Bellingham, WA.
- Prager, R. W., Rohling, R., Gee, A. and Berman, L. (1998a) Rapid calibration for 3-D free-hand ultrasound. *Ultrasound Med. Biol.*, 24, 855–869.
- Prager, R. W., Gee, A. H. and Berman, L. (1999) Stradx: real-time acquisition and visualization of freehand three-dimensional ultrasound. *Med. Image Anal.*, 3, 129–140.
- Rohling, R., Gee, A. and Berman, L. (1997) 3-D spatial compounding of ultrasound images. *Med. Image Anal.*, 1, 177–193.
- Shepard, D. (1968) A two-dimensional interpolation function for irregularly spaced data. In *23rd Nat. Conf. ACM*, pp. 517–523.
- Talmi, A. and Gilat, G. (1977) Method for smooth approximation of data. *J. Comput. Phys.*, 23, 93–123.

- Terzopoulos, D. (1986) Regularization of inverse problems involving discontinuities. *IEEE Trans. PAMI*, 8, 413–424.
- Terzopoulos, D. (1988) The computation of visible-surface representations. *IEEE Trans. PAMI*, 10, 417–438.
- Trobaugh, J. W., Trobaugh, D. J. and Richard, W. D. (1994) Three-dimensional imaging with stereotactic ultrasonography. *Comput. Med. Imag. Graph.*, 18, 315–323.